AGU ADVANCING EARTH AND SPACE SCIENCES

JGR Atmospheres

Key Points:
- Large eddy simulations with the EULAG research model of the atmospheric boundary layer over stochastic lake landscapes
- Lake areal fraction has significant impact on land-atmosphere energy exchange
- Longer surface correlation length causes higher blending altitude

Correspondence to:
M. Schlutow,
mark.schlutow@bgc-jena.mpg.de

Author Contributions:
Conceptualization: M. Schlutow, M. Göckede
Formal analysis: M. Schlutow, T. Stacke
Funding acquisition: M. Göckede
Investigation: M. Schlutow, T. Stacke
Methodology: M. Schlutow, T. Stacke, P. K. Smolarkiewicz
Project administration: M. Göckede
Software: T. Doerffel, P. K. Smolarkiewicz
Supervision: M. Göckede
Visualization: M. Schlutow
Writing – original draft: M. Schlutow
Writing – review & editing: T. Stacke, T. Doerffel, P. K. Smolarkiewicz, M. Göckede

Large Eddy Simulations of the Interaction Between the Atmospheric Boundary Layer and Degrading Arctic Permafrost

M. Schlutow[1], **T. Stacke[2]**, **T. Doerffel[3]**, **P. K. Smolarkiewicz[4]**, and **M. Göckede[1]**

[1]Department Biogeochemical Signals, Max Planck Institute for Biogeochemistry, Jena, Germany, [2]Department Climate Dynamics, Max Planck Institute for Meteorology, Hamburg, Germany, [3]Weierstrass Institute for Applied Analysis and Stochastics (WIAS), Berlin, Germany, [4]NSF National Center for Atmospheric Research, Boulder, CO, USA

Abstract Arctic permafrost thaw holds the potential to drastically alter the Earth's surface in Northern high latitudes. We utilize high-resolution large eddy simulations to investigate the impact of the changing surfaces onto the neutrally stratified atmospheric boundary layer (ABL). A stochastic surface model based on Gaussian Random Fields modeling typical permafrost landscapes is established in terms of two land cover classes: grass land and open water bodies, which exhibit different surface roughness length and surface sensible heat flux. A set of experiments is conducted where two parameters, the lake areal fraction and the surface correlation length, are varied to study the sensitivity of the boundary layer with respect to surface heterogeneity. Our key findings from the simulations are the following: The lake areal fraction has a substantial impact on the aggregated sensible heat flux at the blending height where surface heterogeneities become horizontally homogenized. The larger the lake areal fraction, the smaller the sensible heat flux. This result gives rise to a potential feedback mechanism. When the Arctic dries due to climate heating, the interaction with the ABL may accelerate permafrost thaw. Furthermore, the blending height shows significant dependency on the correlation length of the surface features. A longer surface correlation length causes an increased blending height. This finding is of relevance for land surface models concerned with Arctic permafrost as they usually do not consider a heterogeneity metric comparable to the surface correlation length.

Plain Language Summary The study explores how thawing permafrost (frozen soil) could change the Earth's surface in the Arctic region. The researchers used advanced simulations to study how different types of surfaces, like grassland and lakes, affect the atmosphere above. They found that the proportion of lakes in the area has a big impact on the heat exchange with the atmosphere, suggesting a potential feedback mechanism: as the Arctic dries due to climate change, it might speed up permafrost thaw. Additionally, the study highlights that the arrangement of surface features matters, which is important for models predicting permafrost changes in the Arctic.

1. Introduction

Arctic permafrost is highly vulnerable to climate change, and widespread enhanced thawing can be expected under climate warming. In the process, vast amounts of organic carbon that is currently stored in deep-frozen soil layers may be released from the permafrost carbon pool into the atmosphere, mostly in form of the greenhouse gases CO_2 and CH_4 (Miner et al., 2022; Smith et al., 2022). The current permafrost carbon pool is estimated to contain approximately 1,440–1,600 Pg of carbon, which is more than double the amount already present in the atmosphere (Mishra et al., 2021; Schuur & Mack, 2018). The positive feedback mechanism of accelerated thaw in combination with increased carbon emission, further enhancing atmospheric greenhouse gas levels and thus warming rates, was identified to be among the six most likely potential tipping elements that might be reached even within the Paris Agreement range of 1.5°C global warming (McKay et al., 2022). Forecasting the fate of the high-latitude frozen soils is extremely challenging because, on the one hand, there is a large uncertainty in our understanding of the mechanics and ecology of permafrost thaw and, on the other hand, Arctic permafrost is not yet well represented in climate models (McGuire et al., 2018; Schuur et al., 2022). These uncertainties, among others, are demonstrated by the fact that most global climate models substantially underestimate the historic temperature increase in the high latitudes, which is about 4 times faster than the global average (Rantanen et al., 2022).
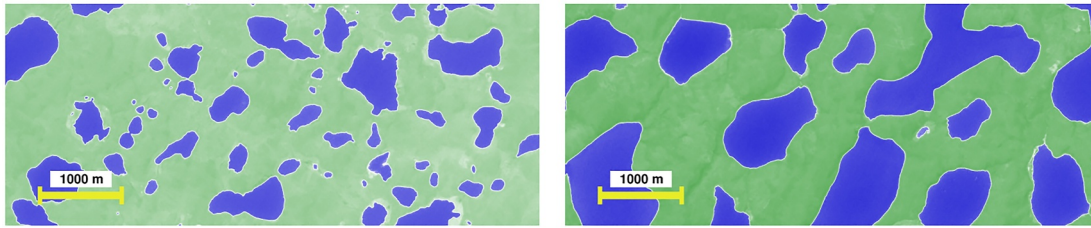
Figure 1. Satellite images of open water bodies (blue areas) in the Mackenzie River delta. The Normalized Difference Water Index (NDWI) derived from Sentinel 2 data available on the Sentinel Hub EO Browser is shown.

Complementary to carbon emissions, Arctic permafrost thaw causes serious alterations to the structure of the land surface. Disturbances like thermokarst and subsidence will lead to changes in topography and related hydrological re-distribution, initializing for example, the formation of ponds and lakes in tundra landscapes (Liljedahl et al., 2016; O'Donnell et al., 2012), or the drainage of lake basins, in all cases with potentially drastic influences on landscape and ecosystem processes (Jones et al., 2022). Also, snow cover dynamics are affected by disturbances (Chen et al., 2016; Lupascu et al., 2014), which contributes to a changing vegetation structure.

It can be expected that these surface alterations substantially affect the circulation in the atmospheric boundary layer (ABL). Various vegetation types covering the surface, like for example, grasses and shrubs as well as open water bodies, exhibit different characteristics of energy exchange between the surface and the atmosphere (Foken, 2008). Their fractional coverage within a landscape therefore leads to distinct ABL properties, and furthermore also the spatial distribution of surface features, their structure forming landscape heterogeneity, has a potential effect on the submeso-scale flow. Figure 1 displays typical surfaces of tundra landscapes and the range of different spatial scales involved.

To study the ABL over heterogeneous Arctic permafrost landscapes and potential feedbacks, large eddy simulations (LES) are a particularly beneficial resource. Idealized LES experiments with altering regular stripes of different roughness were conducted by for example, Bou-Zeid et al. (2004). Michaelis et al. (2020) used LES to study the formation of thermals as well as their impact on the boundary layer height due to leads in Arctic sea ice where also regular patterns represented the heterogeneous surface. Maronga and Raasch (2013) investigated the influence of an inhomogeneous surface covered with a dense in situ observational network on the convective boundary layer during the LITFASS-2003 experiment in temperate latitudes. A stochastic model for surface features in combination with LES of typical crop lands was utilized by Huang and Margulis (2009). Their model generates idealized irregular random surface patterns governed by the surface correlation length. Furthermore, Sühring and Raasch (2013) studied the impact of heterogeneity on the blending height which is the theoretical threshold altitude above which the inhomogeneity of the surface becomes horizontally blended when considering fluxes. This important concept is also of significance for surface parametrizations in Earth System Modeling.

One of the challenges for land surface models is to represent surface heterogeneity at fine spatial scales in the Arctic, since the dominant length scales are usually much smaller than the model's spatial resolution. To retain at least a basic representation of subgrid-scale heterogeneity in these models, a common technique is tiling, where several different land-cover types can occupy a specific fraction of the grid box area (Blyth et al., 2021; Bou-Zeid et al., 2020). However, the aforementioned surface correlation length is completely independent from the areal fraction of a surface feature, and instead determined by the typical patch size and the spatial arrangement of different land cover units. In land surface models the surface correlation length is commonly not considered as an input parameter. In other words, a model may have information about the total lake area within a tile, but it cannot consider if the area is divided into many small lakes or one big lake, as this kind of information is contained in metrics like the surface correlation length.

Despite the multitude of carefully conducted investigations of surface heterogeneities within manifold land cover classes with LES, little is known about the impact of the inhomogeneous Arctic permafrost landscape onto the ABL structure. This question is of particular relevance considering the extensive land surface area underlain by permafrost in the Arctic region, and its rapid change in the context of Arctic warming, which may lead to potential feedback mechanisms. To address this problem, in this study we conduct LES experiments over idealized stochastic landscapes that are typical for permafrost, thermokarst or thaw lake formation, and statistically analyze the

effects of landscape structure on the ABL dynamics. The study is structured as follows. In Section 2 we introduce the LES model and a stochastic land cover model which utilizes two parameters defining the heterogeneity: the lake areal fraction and the surface correlation length. The model configuration and the methods for statistical analysis will be presented. In Section 3, we will show and discuss a reference simulation that is also used for model validation purposes. Next, a parameter sweep (or sensitivity) experiment will be conducted where the two parameters that govern the surface heterogeneity are varied. We analyze the reaction of the ABL to these changes, with a particular focus on blending properties, and a discussion on how these results affect the land-atmosphere interaction models in Earth System Models (ESM) in the permafrost region. Some concluding remarks on the implications and potential feedback mechanisms as well as an outlook for future studies will be given in Section 4.

2. Methodology

In what follows, the basis for numerical experiments to investigate the boundary layer of the atmosphere above stochastic permafrost landscapes is established.

2.1. The Large Eddy Simulation Model

We utilize the EULAG (Eulerian–Lagrangian) research model for our purposes. It is an established all-scale numerical model for atmospheric dynamics, that is, low Mach number, high Reynolds number, stratified flows under gravity. A comprehensive overview of EULAG can be found in Smolarkiewicz et al. (2014); Piotrowski and Smolarkiewicz (2022). A soundproof version of the Euler equations, comprised of the conservation laws for dry mass, momentum and entropy are advanced in time with a semi-implicit integrator. The integrator takes advantage of the multidimensional positive definite advection transport algorithm (MPDATA) for atmospheric flows (Smolarkiewicz, 2006). For turbulence closure, the prognostic equation for the Turbulent Kinetic Energy (TKE) is solved in addition to the resolved state variables, and a dynamic Smagorinsky model is applied where the eddy viscosity is parametrized by means of TKE (Schumann, 1991; Sorbjan, 1996). The full equations of the turbulence closure model and details on their implementation can be found in (Margolin et al., 1999, Section 2, Appendix A).

Subgrid-scale effects of roughness of the land surface are modeled with Monin-Obukhov similarity theory (MOST) for neutral stability conditions at the lowest model layer (Sorbjan, 1996) whereas the sensible heat flux forces the flow in the model on the resolved scales. EULAG has been tested extensively against ideal flow test case suites, wind channel flows and real-life observations (Dörffel et al., 2021; Kurowski et al., 2016; Piotrowski & Smolarkiewicz, 2022; Smolarkiewicz et al., 2007).

2.2. The Land Cover Model

A stochastic land cover model for Arctic tundra landscapes is proposed that is easy to implement and has beneficial properties to investigate the impact on the ABL due to altering heterogeneities. Since the goal of this study are idealized experiments focusing on the spatial distribution of surface features, the model contains only two land cover classes: open water body and grass. The key idea of the model is to use excursion sets of Gaussian Random Fields (GRFs), that is, smooth, continuous fields similar to topographic maps, to generate artificial maps of terrain height. Land cover maps are obtained in terms of GRFs by selecting a threshold value and define all points with a value of the field above the threshold to be grass land and every point with a value below the threshold to be open water bodies. The collection of points defined in this way are called excursion sets (Ostwald et al., 2021), and the smoothness of the GRF guaranties smooth lake shores.

Here, we reproduce the method as presented in Heße et al. (2014), who also give a detailed overview on the matter, to generate a GRF. It starts with the spectral density function S that defines the overall shape of the lakes and a surface correlation length λ which can be seen as an average distance between lakes. The spectral density function can be derived from the variogram of the landscape which might be obtained from satellite imagery (Wackernagel, 1995). As variograms for tundra landscapes are, to our knowledge, not available in the literature, we assume a Gaussian variogram which results in a Gaussian spectral density function like

$$S(\boldsymbol{k}, \lambda) = \left(\frac{\lambda}{\pi}\right)^2 e^{-(|\boldsymbol{k}|\lambda)^2/\pi} \tag{1}$$

where k has units of inverse length.

Given the respective horizontal domain length in zonal and meridional directions as L_x and L_y and some numbers $Z_{i,j}^{(d)} \sim \mathcal{N}(0,1)$ from the unit normal distribution, we can generate a GRF in terms of a Fourier series as

$$g(x) = \sqrt{\frac{2}{L_x L_y}} \sum_i \sum_j \sqrt{S(k_{i,j})} \left[Z_{i,j}^{(1)} \cos(2\pi k_{i,j} \cdot x) + Z_{i,j}^{(2)} \sin(2\pi k_{i,j} \cdot x) \right]. \tag{2}$$

The vector $x = (x, y)$ lies in the horizontal plane. The vector $k_{i,j}$ is a discretization of k. Please note that by construction the GRF is periodic in both horizontal directions. Therefore, we are able to tessellate an infinite continuous tundra periodically. An open water body is now defined as all points x for which $g(x) < g_q$ where the subscript q denotes the lake areal fraction.

Since the distribution of g is also Gaussian—hence the name—the number g_q is the inverse of the cumulative distribution function (CDF), where q is the quantile representing the relative amount of open water in the entire domain that is otherwise covered with grass. To compute the inverse of the CDF, we might use an approximation given in Abramowitz and Stegun (1972). However, we solve for g_q numerically by sorting all values of $g(x)$ on the discrete grid which yields a vector of length nm and evaluate its value at $\lfloor qnm \rfloor$ where $\lfloor \cdot \rfloor$ denotes the floor function and n,m are the numbers of grid points in each direction.

Representative fluxes of sensible heat and roughness lengths for tundra grasslands and open water bodies, respectively, were computed in a coupled land-atmosphere simulation using the ICON-ESM (Jungclaus et al., 2022), an Earth System Model developed at the Max Planck Institute for Meteorology, the German Weather Service, and other partner institutions. With the use of ICON-ESM it is possible to provide fluxes for the individual land cover classes. Given the short timescales of interest, ICON-ESM was run with prescribed fields of observed sea surface temperature and sea ice concentration, rather than coupling to an interactive ocean model. As land surface component, we used the ICON-LAND framework (Schneck et al., 2022) including a port of the JSBACH (Reick et al., 2021) land surface model. From this simulation, 1 month of simulation data was extracted for one grid cell during boreal summer. The grid cell was selected based on its general location in the high-northern latitudes in combination with covering the required land surface classes at 68.40° North, 151.18° East. The exact time step to be used as forcing for EULAG was determined based on the simulated atmospheric stability.

ICON-ESM uses an implicit coupling approach for interactions between the land surface and the vertical diffusion scheme within the atmosphere component. Based on coefficients representing the vertical relation of heat and moisture within the atmospheric column, ICON-LAND solves the land surface energy balance. This provides the lower boundary conditions for saturated humidity and dry static energy, which are then used to iteratively compute the specific humidity and dry static energy of each atmospheric layer. In the process, sensible heat flux is computed as the product of the heat exchange coefficient between land surface and the lowest atmospheric layer and the difference in the respective dry static energy values at both locations. Surface roughness is computed individually for specific surface types and aggregated afterward. It employs the idea of the blending height concept and distinguishes different surface conditions (snow-covered, snow-free bare soil and snow-free vegetated surfaces). The full set of equations regarding the implementation of the surface energy balance and coupling to the atmosphere can be found in Reick et al. (2021).

2.3. Model Configuration

EULAG provides the option to choose from the compressible model or versions of soundproof models such as the pseudo-incompressible (Durran, 1989), anelastic (Lipps & Hemler, 1982) or classical incompressible Boussinesq model (Achatz et al., 2010; Davies et al., 2003; Klein et al., 2010). In this work the Boussinesq model is chosen. Since the vertical model extent $L_z = 500$ m is much smaller than the typical scale height, we would not expect much differences in the results with respect to the other, more accurate, model configurations. The Boussinesq version is considerably faster. In the lateral direction the boundary conditions are periodic, that is, every outflow on the right-hand-side boundary would re-enter the domain from the left. A drawback resulting from this choice are the potential formation of artificial periodic patterns. How these patterns form, and how we prevented their formation will be discussed in Section 3.1.

Table 1
Surface Model Specifications

Land cover type	Sensible heat flux [Wm^{-2}]	Roughness length [m]
Open water body	−27	0.001
Grass land	310	0.16

At the top boundary a "moving sponge/absorber" is applied: above 400 m a Rayleigh damping scheme is implemented (Durran & Klemp, 1983) that acts only on the horizontal wind and relaxes the flow to the geostrophic wind u_g. The latter is at an angle β_g to the *x*-axis. The choice of this angle and also the choice of the elongated domain will be justified in Section 3.1. At the surface the shear-stress is derived from the roughness of grass land and open water bodies, respectively, which were computed by means of JSBACH as discussed above. Their values can be found in Table 1. For the geostrophic wind we chose a typical value for the Arctic based on the theoretical thermal wind balance at 68° North. Since the wind is strong enough and our domain considerably large, we can expect an influence of the Coriolis force at high latitudes which is therefore engaged in EULAG. In conclusion, the ABL dynamics is driven by both shear and convection.

The background temperature is such that the ABL is neutrally stratified, that is, isentropic, which models a typical sunny noon. The surface temperature of the background is 0 °C. For the initial conditions of the simulations, the horizontal wind is set to a logarithmic profile derived from MOST plus additional noise to trigger instabilities and, thus, turbulence. The vertical wind and the potential temperature perturbation from the background are initially zero. In order to obtain a realistic and fully developed turbulent field, the domain is discretized isotropically with cell sizes $\delta x = \delta y = \delta z$. From the initial laminar condition, the model is run for 12 hr which proved to be long enough to yield a turbulent field with stationary statistics. Note that the surface sensible heat flux is kept constant to ensure stationarity implying that our experiments do not allow for a diurnal cycle. In these spin-up runs, the time step is adaptive and automatically computed from the current wind field such that the Courant number (C) can be chosen as large as to assure numerical stability. The adaptivity allows for the largest possible time steps.

After the spin-up we run the model for an additional hour to compute temporal averages of relevant fields and fluxes. How the averaging was applied to different variables will be discussed in Section 2.4. All fixed model parameters, that are kept constant throughout all experiments, can be found in Table 2.

We computed the typical lake areal fraction q and the surface correlation length λ for the stochastic generation of the land covers in (2) based on the results in Muster et al. (2019), who analyzed the data from the circum-Arctic Permafrost Region Pond and Lake (PeRL) project. The mean surface correlation length from this data set is $\lambda \approx 300$ m and the mean lake areal fraction is $q \approx 10\,\%$. We consider the land cover originating from these two numbers as the reference case. Simulation results of the ABL over the reference land cover will be shown in the next section.

Next, we vary the lake areal fraction and the surface correlation length in a parameter sweep experiment within the ranges provided by Muster et al. (2019). The corresponding land cover maps are presented in Figures 2 and 3. Also, an overview of the experiments with corresponding statistics like mean lake area and mean number of lakes per square kilometer are found in the Appendix in Table A1. Figure 2 displays the changing land covers for the parameter sweep where we keep the surface correlation length fixed and vary the lake areal fraction. This experiment may represent permafrost tundra wetting where the spatial scales are fixed, and the water table rises to progressively inundate larger areas. The land cover maps for constant lake areal fraction and altering surface correlation length are shown in Figure 3. This experiment simulates a scenario where permafrost degradation reshapes the topography by, for example, subsidence to progressively form larger lakes, therefore providing an interesting test ground for quantifying structure effects on the performance of land surface models (like JSBACH). In our study, we analyze the influence of surface structure on the sensible heat flux and the friction temperature, which are import outputs of land surface models. For all experiments, the roughness length and the sensible heat flux for grass land and open water body are kept constant. Their respective values are given in Table 1.

Table 2
Fixed Model Parameters

Domain size	$L_x \times L_y \times L_z$ [m^3]	$1000 \times 4000 \times 500$
Grid size	$\delta x \times \delta y \times \delta z$ [m^3]	$3.9 \times 3.9 \times 3.9$
Number of grid points	$n \times m \times l$	$256 \times 1024 \times 128$
Time step	δt [s]	~0.2
Courant number	C	0.9
Geostrophic wind	u_g [m/s]	7.0
Wind angle	β_g [°]	17.0

2.4. Statistical Analysis

After a 12 hr model spin-up, we restart the model with the final state of the spin-up run as initial condition, and average over 1 hour taking every time step into account. Due to the nature of the turbulent field assumed being
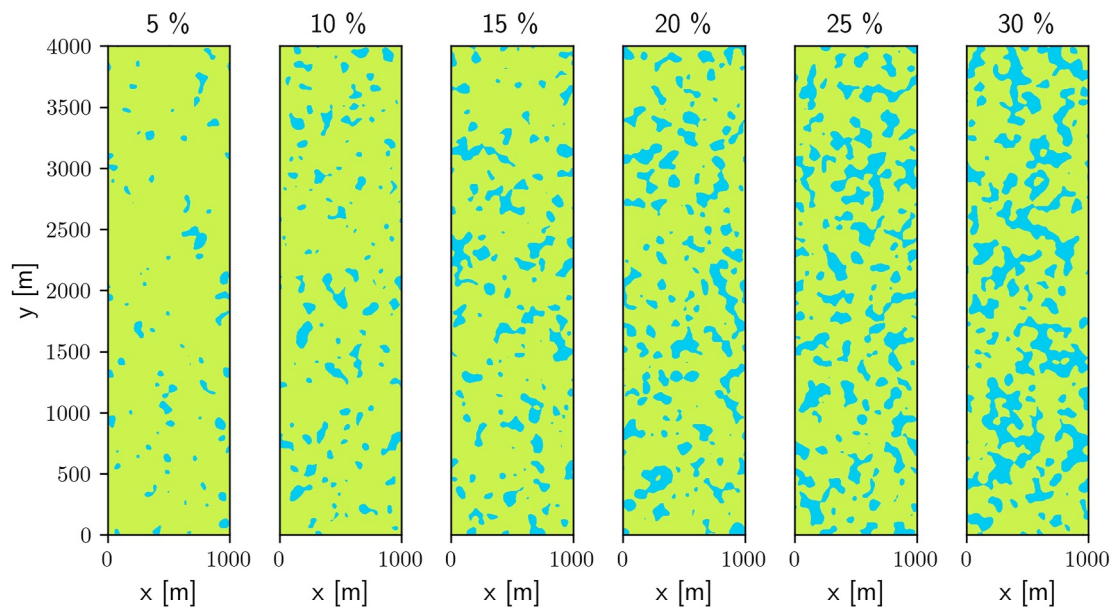
Figure 2. Land cover maps with constant surface correlation length of 300 m and varying lake areal fraction. Green displays grass land and blue is open water bodies.

ergodic, the temporal average ($\bar{\cdot}$) can be regarded as Reynolds-type ensemble averaging. The turbulent vertical flux of any variable like potential temperature or momentum, $\{\theta, u, v, w\} \ni \phi = \bar{\phi} + \phi'$ is computed during run-time taking advantage of the decomposition

$$\overline{w'\phi'} = \overline{w\phi} - \bar{w}\bar{\phi} \tag{3}$$

where w denotes the vertical wind component, cf. Sühring and Raasch (2013). By means of this method, the average of a particular quantity and its flux are computed concurrently. The average yields spatially heterogeneous fields regarded collectively as the secondary circulation.

Defining the spatial average at a certain height as $\langle \cdot \rangle$, the sensible heat flux at 30 m altitude is then computed as
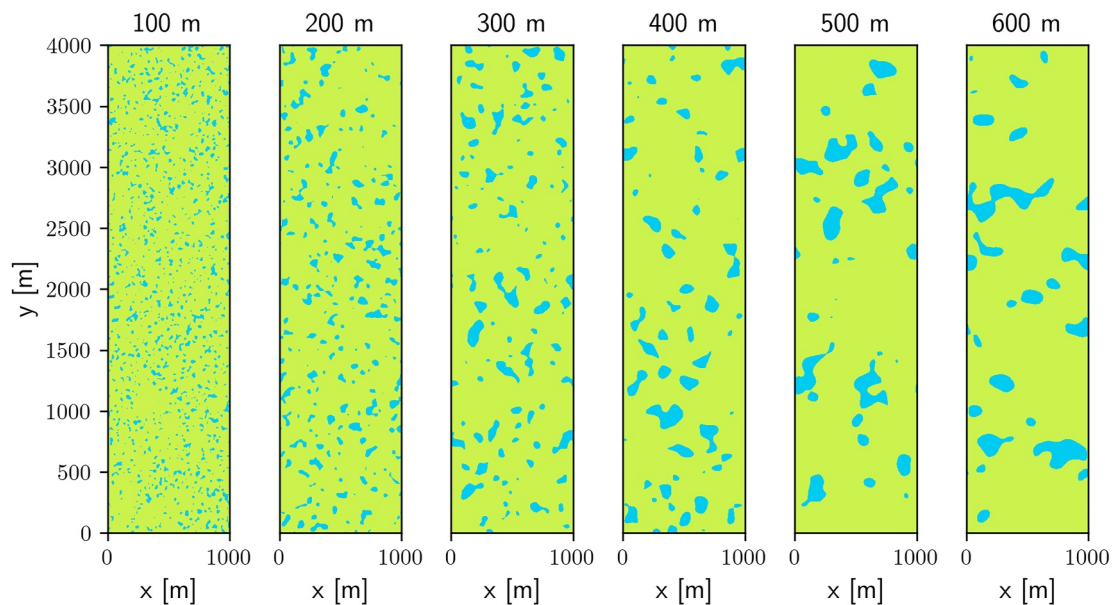

Figure 3. Land cover maps with constant lake areal fraction of 10% and varying surface correlation length. Green displays grass land and blue is open water bodies.

$$\langle H_{30} \rangle = c_p \rho_r \langle \overline{w' \theta'} \rangle. \tag{4}$$

Heat capacity at constant pressure and reference density are given as c_p and ρ_r, respectively. The particular altitude of 30 m is of interest as it is a typical height for the lowest model layer of the atmospheric module of climate models. Whether or not the spatial average can be considered a valid mean in the statistical sense depends on the blending height (Mahrt, 2000). The blending height may be defined as the height above the surface at which the influence of the heterogeneous surface on a given quantity becomes insignificant. In order to investigate the dependence of the flow structure at a certain height on the surface heterogeneity and constrain the blending height, we compute the two-dimensional normed spatial cross-correlation function (SCCF) between the sensible heat fluxes at the ground and at 30 m (Lohou et al., 1998),

$$\varrho_{0,\,30}(\Delta x, \Delta y) = \frac{(H_0 - \langle H_0 \rangle) * (H_{30} - \langle H_{30} \rangle)}{\sqrt{\langle (H_0 - \langle H_0 \rangle)^2 \rangle \langle (H_{30} - \langle H_{30} \rangle)^2 \rangle}}. \tag{5}$$

Here, $*$ stands for the 2-dimensional convolution function and $\langle H_0 \rangle$ is the surface sensible heat flux. Please note that $-1 < \varrho_{0,\,30} < 1$ is equivalent to the spatially dependent Pearson correlation coefficient. When the cross-correlation vanishes, that is, the flow at 30 m is spatially uncorrelated with the surface, we may consider the level to be above the blending height. In reality, it will never vanish completely but drop below a certain threshold that needs to be determined for the specific application.

Furthermore, we compute the friction velocity squared as

$$u_*^2 = \sqrt{\langle \overline{u' w'} \rangle^2 + \langle \overline{v' w'} \rangle^2} \tag{6}$$

and the friction temperature as

$$\theta_* = -\frac{\langle \overline{w' \theta'} \rangle}{u_*} \tag{7}$$

at $z = 30$ m as metrics for turbulent transport and motivated by the fact that friction velocity and friction temperature are key parameters in turbulent closure models like MOST. Notice that, strictly speaking, the averaged fields as presented above do not amount to all of the turbulence, that would typically be present in such a boundary layer flow. This is because only the resolved part of the fluctuations are considered in the simulations. Therefore, it needs to be ensured that most of the turbulent spectrum materializes on the resolved scale in order to draw statistical conclusions. Taken this argument into account the spatial resolution of ~ 4 m for the simulations was chosen (see Table 2).

3. Results and Discussion

Based on the model configurations as discussed above, simulation results are presented in the following sections. First, we consider a reference simulation to illustrate the flow properties and to corroborate the physical validity of the simulation. Second, a parameter sweep is performed testing the sensitivity of the system with regard to surface heterogeneity typical for Arctic permafrost tundra landscapes.

3.1. The Reference Simulation Q10L300

We consider the LES run with the parameter setting of surface correlation length, $\lambda = 300$ m and lake areal fraction, $q = 10\%$ as our reference simulation (Q10L300) since those values represent the most typical landscape in Muster et al. (2019). Figure 4 shows the zonal wind (parallel to the x-axis) after 12 hr simulation time for the Q10L300 case. Along with the momentary fully turbulent field, the temporally averaged field is displayed. The latter constitutes the secondary circulation, when all turbulence is removed. From both, the turbulent and secondary zonal wind in Figure 4, it can be observed that the flow is considerably slower over the grass patches (green areas) than over water (blue areas). This observation is explainable with the higher roughness length of
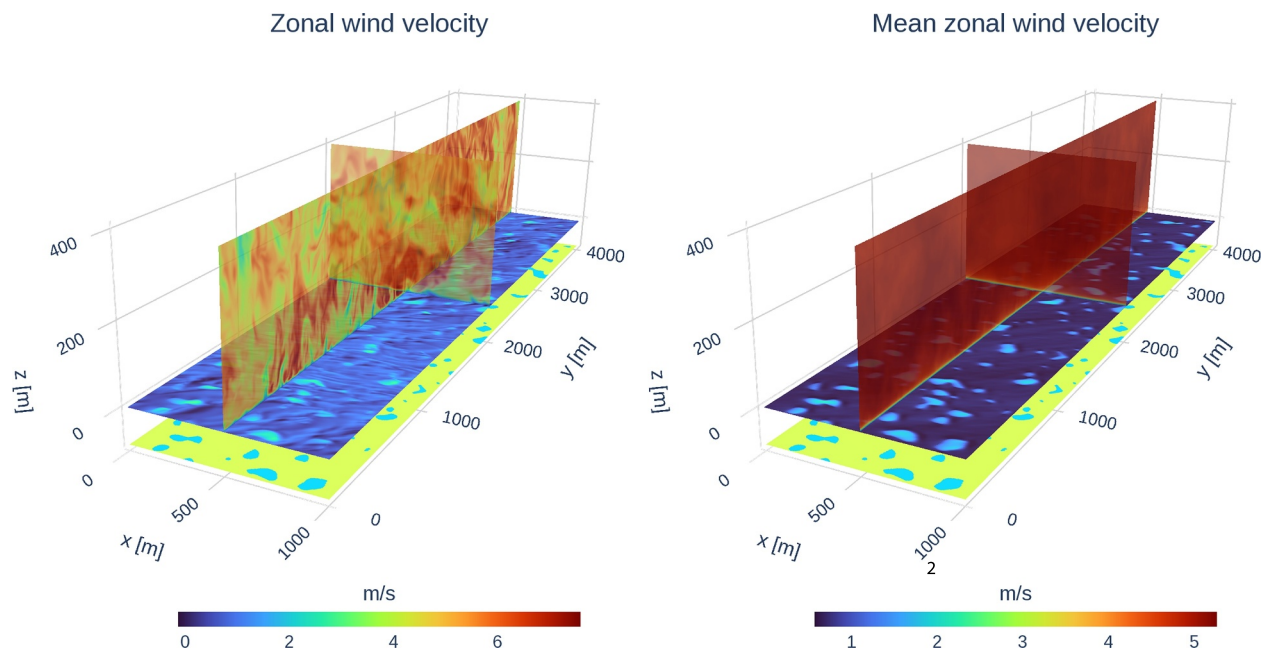
Figure 4. Zonal wind velocity after 12 hr spin-up from the Q10L300 case. Panels show the turbulent field (left) and the temporally averaged secondary circulation field (right). The horizontal slice displays the lowest model layer. The corresponding land cover map is displayed at the bottom.

grass in comparison with water (see Table 1) which causes a greater surface stress. From the averaged field it can be seen that the wind velocity increases with height. Figure 5 displays the vertical profiles of mean horizontal as well as vertical wind, potential temperature and kinematic heat flux. The profiles have the expected shape as for example, given in (Deardorff, 1974). In the leftmost panel, the vertical profile of the averaged horizontal wind resembles the typical logarithmic dependency in the lowest 150 m as expected from MOST.

The turbulent and secondary vertical wind fields are shown in Figure 6. In the turbulent field, large-scale up- and downdrafts can be observed, respectively, which are due to the aggregated heating at the ground and resemble thermal plumes. The eddies become smaller closer to the surface, which is also in line with MOST. We notice that the thermals sometimes exceed 2 ms^{-1} in vertical velocity, which is not untypical for sunny conditions in the Arctic summer. As has been seen in the zonal wind, the flow over the lakes accelerates, and therefore the pressure drops. Assuming incompressibility or solenoidality of the wind field, respectively, which is valid for submeso-scale flows, it can be reasoned that a downdraft must be generated at the wind-ward lake shores and an up-draft in the leeward shores. The resulting pattern is manifested in the mean vertical wind (see lowest horizontal slice in the right panel of Figure 6). As to be expected, the mean of the vertical wind is negligible (see Figure 5). Also note that the secondary circulation is not spatially homogeneous. Imprints from the surface heterogeneity remain seemingly visible throughout the vertical column. An open question at this point is whether those imprints at higher layers are statistically relevant, which will be discussed in more detail in the following Section 3.2.

Further note that the size and shape of our domain in combination with the periodic lateral boundary conditions limits the degrees of freedoms of the system and, therefore, favors particular flow patterns. To suppress these artificial patterns, we opted for an elongated domain and an angle between the mean wind and the x-axis other than $0°$ or $90°$. Experiments with $\beta_g = 90°$ resulted in a secondary circulation with one stretched overturning eddy with the size of the domain (not shown here). An angle of $\beta_g = 17°$ in combination with a rectangular base area proved to suppress this artificial mode successfully.

In order to further quantify the impact of the secondary circulation on the results of the statistical analysis, we investigate the dispersive heat flux and its contribution to the total flux. Dispersive fluxes appear due to secondary circulations as an additional term in the averaged governing equations when temporal mean variables are also spatially averaged, cf. our Equation 4. Margairaz et al. (2020) showed that—under certain flow regimes—dispersive fluxes can account for more than 40% of the total heat flux. Since (4) does not account for the
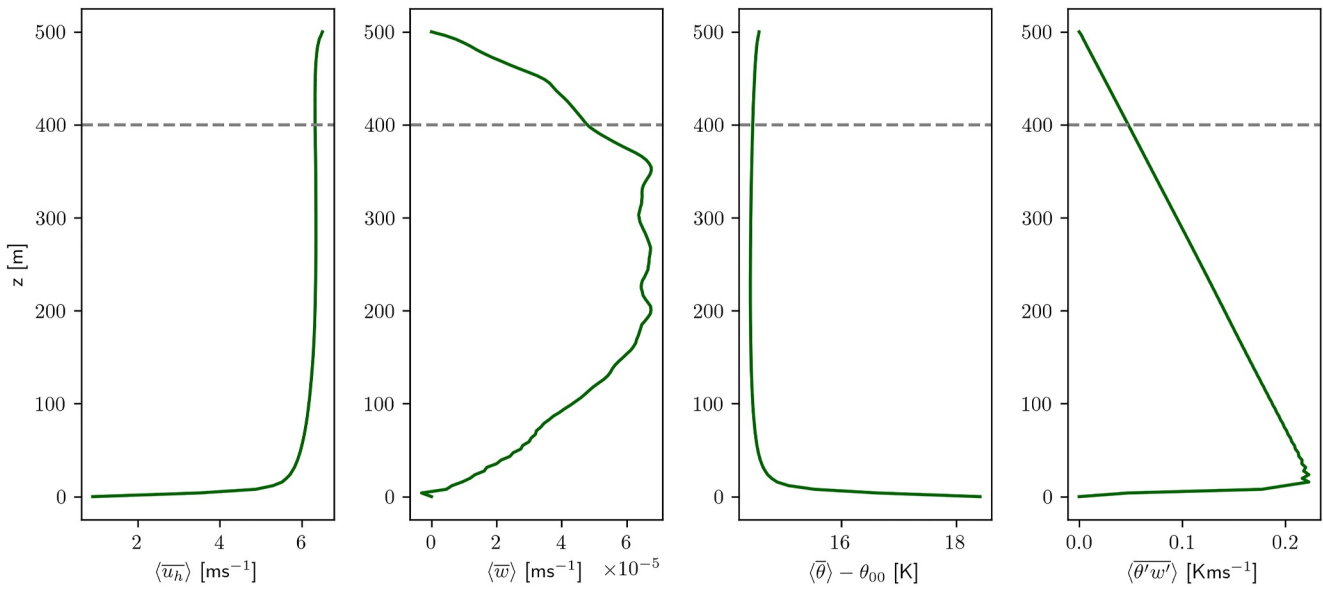
Figure 5. Vertical profiles of temporally and horizontally averaged horizontal wind, vertical wind, potential temperature and kinematic heat flux. The gray dashed line at 400 m marks the beginning of the "moving sponge" layer.

dispersive heat flux, the secondary circulation presents a potential source of ambiguity in our simulations. However, LES results from Margairaz et al. (2020, their Figures 4 and 5) suggest that strong geostrophic winds and long averaging times minimize the effect. Based on these results, we can expect for the flow regime in our simulations that the contribution from the dispersive fluxes is less than 5% which lies within acceptable margins.

Figure 7 shows the turbulent and temporally averaged potential temperature offset by the reference value $\theta_{00} = 273.15$ K. In the turbulent field, thermals can also be observed. The horizontal slice closest to the surface in the mean field showing the lowest model layer clearly reflects the land cover pattern as the air over the open water
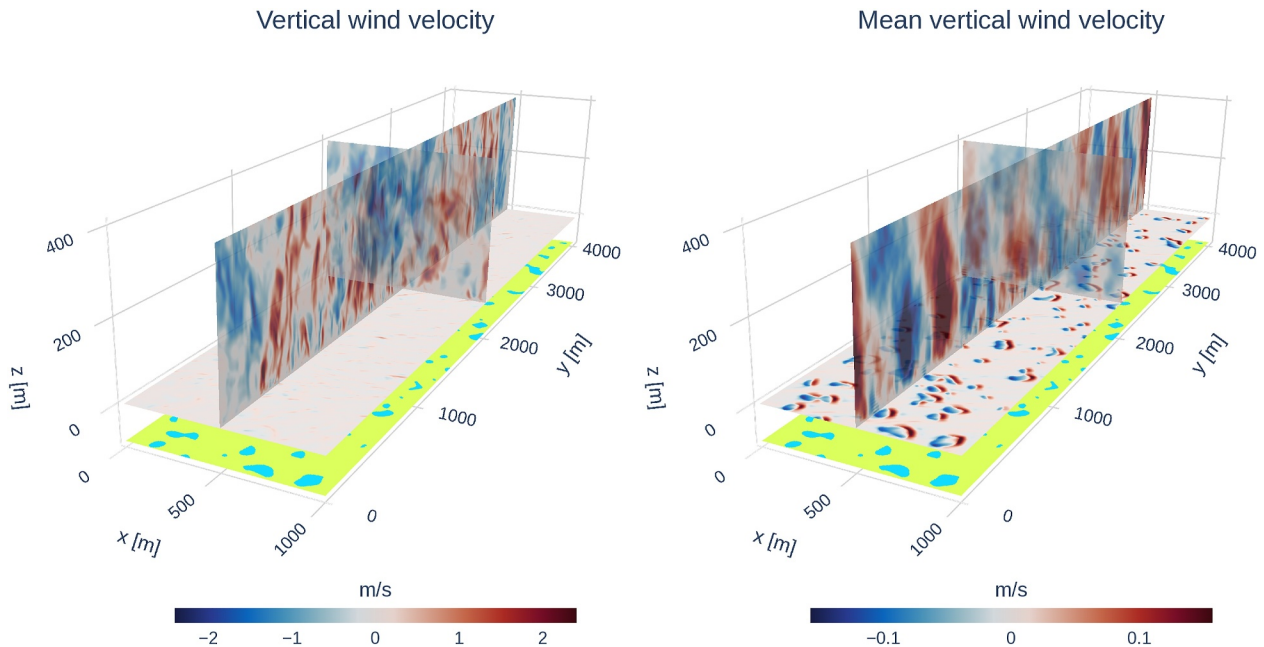

Figure 6. Vertical wind velocity after 12 hr spin-up from the Q10L300 case. Turbulent field (left) and temporally averaged secondary circulation field (right). The horizontal slice displays the lowest model layer. The corresponding land cover map is displayed at the bottom.
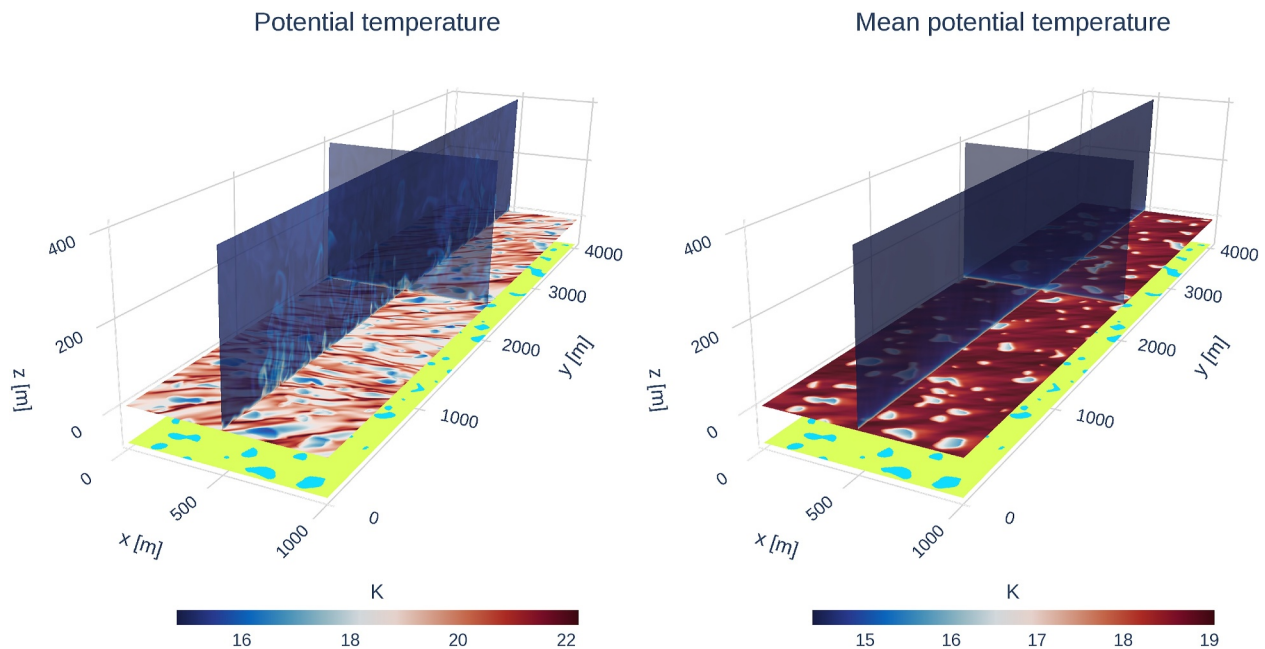
Figure 7. Potential temperature after 12 hr spin-up from the Q10L300 case. Panels show the turbulent field (left) and the temporally averaged secondary circulation field (right). The horizontal slice displays the lowest model layer. The corresponding land cover map is displayed at the bottom.

bodies is cooled, while it is heated over the grass patches. The vertical profile of the mean potential temperature along with the kinematic heat flux can be found in Figure 5.

We conclude this subsection by additional corroboration of the physical validity of the reference simulation in terms of the power spectral density. The latter may be interpreted as the kinetic energy binned with respect to the turbulent eddy size. We found the spectra as expected from theory for our simulations showing that, indeed, the majority of the turbulent spectrum materializes on the resolved scale. These results are displayed in Appendix B.

3.2. Parameter Sweep

In order to find out how the ABL reacts to variations of the heterogeneity parameters q and λ, a sensitivity analysis, or parameter sweep, was performed. The results of this exercise are presented in Figures 8 and 9. For the first experiment, the surface correlation length was set constant to 300 m which matches the mean value as discussed in Section 2.3. The lake areal fraction was varied in steps of 2.5% from 5% to 30%. The corresponding land cover maps to this experiment are found in Figure 2. The horizontally and temporally averaged values (see Section 2.4) of friction velocity squared, friction temperature and sensible heat flux at 30 m above the surface depending on the lake areal fraction are shown in Figure 8. Along with the simulation results, a linear best fit curve with area of uncertainty as well as the slope and the Pearson correlation coefficient are presented. Appendix C contains a brief discussion on alternatives to the linear best fit curve. It can be observed from the Pearson correlation coefficient that all three metrics are strongly anti-correlated with the lake areal fraction. The three computed parameters are in the range of the expected predictions from MOST. In particular, the sensible heat flux exhibits a strong variation from $180 \, \mathrm{Wm}^{-2}$ for $q = 30 \, \%$ up to $255 \, \mathrm{Wm}^{-2}$ for $q = 5 \, \%$ which amounts to a range of variability of about 40%. Since grass has a positive and water a negative surface sensible heat flux, we observe a smaller blended sensible heat flux at 30 m for larger lake areal fraction. The same line of reasoning holds for the friction velocity, u_*. An increased lake areal fraction results in a smaller aggregated surface roughness, as open water bodies have a significantly smaller surface roughness than grass land. A smaller surface roughness yields a diminished surface stress and therefore reduced shear, which induces less turbulence. As a result the vertical transport of horizontal momentum from the model top, and hence u_*, decreases with increasing lake areal fraction.

Figure 9 shows the same horizontally and temporally averaged values as before but for varying surface correlation length and constant lake areal fraction of 10%, which meets the mean value as discussed in Section 2.3. The corresponding land cover maps to this experiment are found in Figure 3. A significant correlation between the
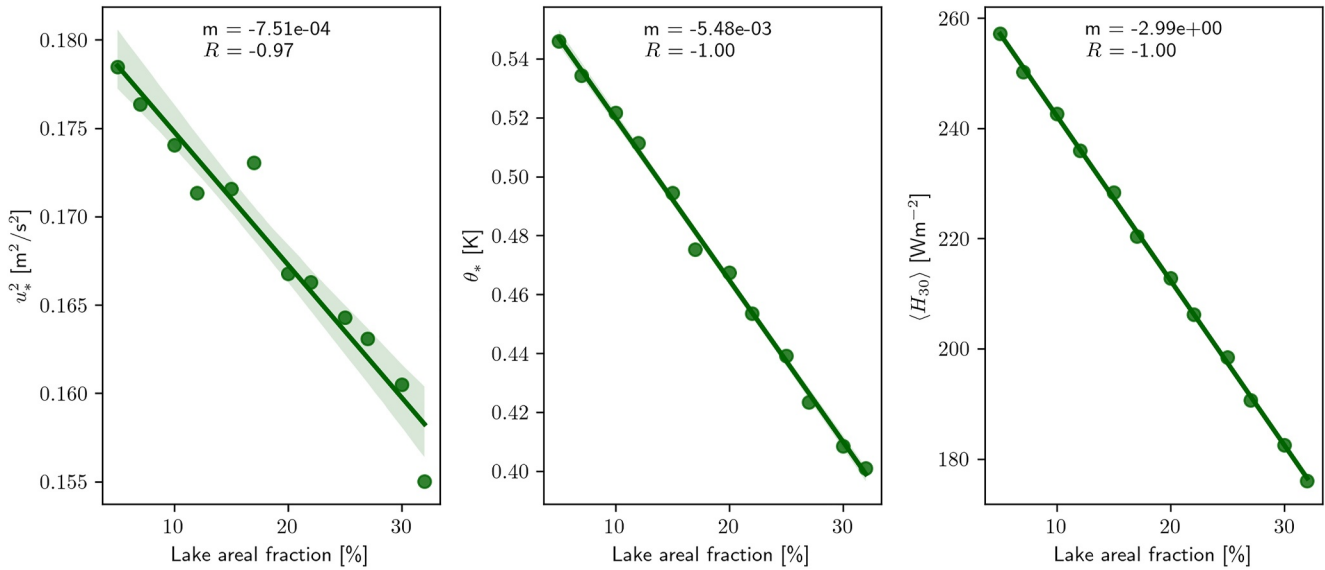
Figure 8. Friction velocity squared, friction temperature and sensible heat flux at 30 m altitude for constant surface correlation length of 300 m. m denotes slope and R the Pearson correlation coefficient.

friction velocity squared and the surface correlation length can be observed with a p-value of $0.013 < 0.05$. Its range of variability is about 8 $m^2 s^{-2}$ (5%). The friction temperature is anti-correlated with the surface correlation length with a p-value of $0.003 < 0.01$ indicating strong evidence. Its range is about 10 K (3%). It can be seen that the sensible heat flux exhibits a moderate anti-correlation with the surface correlation length ($R = -0.50$), albeit at a low significance level ($p = 0.1$). The range in the sensible heat flux is approximately 2 Wm^{-2} (1%).

In this experiment we observe that the friction velocity squared correlates with the surface correlation length. A rudimentary explanation of this feature might be provided by consideration of the mixing length l_m, which was interpreted by Prandtl (1926) as the mean distance of a fluid parcel before it gets mixed and loses its properties. A model assumption in MOST to obtain the eddy viscosity for turbulent flows over homogeneous surfaces is that the mixing length is proportional with height z. Over heterogeneous surfaces, however, it can be expected that the
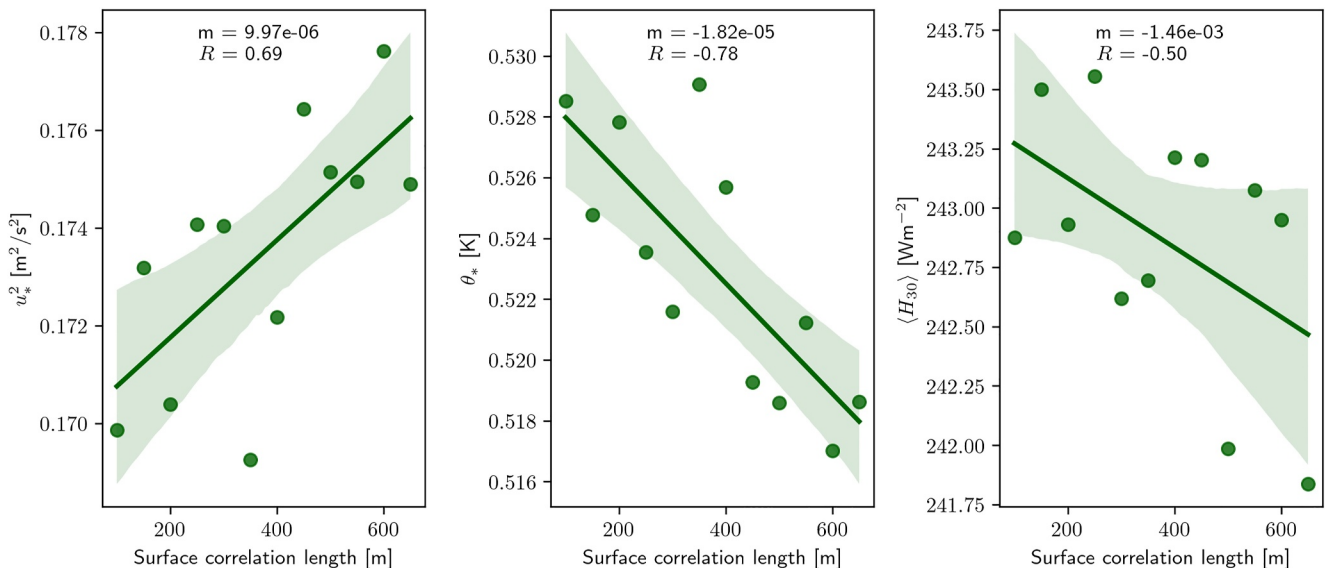

Figure 9. Friction velocity squared, friction temperature and sensible heat flux at 30 m altitude for constant lake areal fraction of 10%. m denotes slope and R the Pearson correlation coefficient.
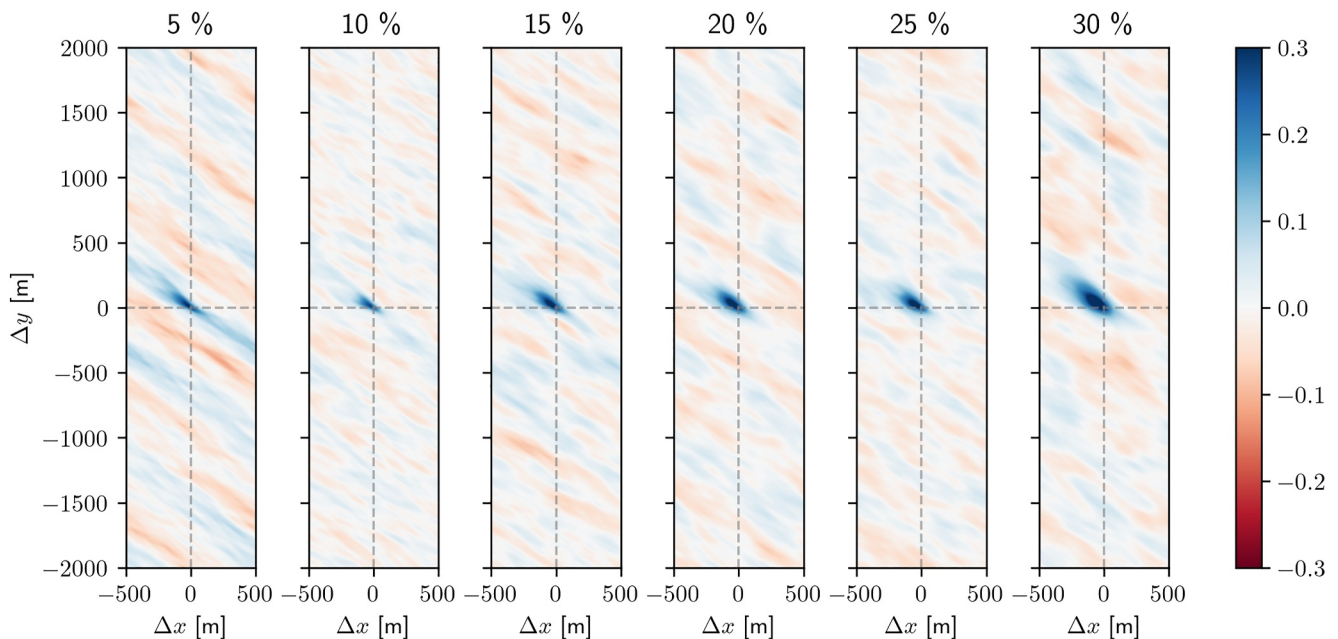
Figure 10. Spatial cross-correlation functions (SCCF) of sensible heat flux at 30 m and the surface, $\varrho_{0,30}$ for large eddy simulations experiments with constant surface correlation length and altering lake areal fraction.

length scale of the heterogeneity, that is, the surface correlation length λ, also influences the mean distance before a parcel gets mixed: the longer the surface correlation length, the longer the free, undisturbed path of the fluid parcel. In the spirit of similarity theory, it is reasonable to assume that $l_m \sim \lambda$ which implies that the eddy viscosity and, therefore, the friction velocity scales with the surface correlation length. This effect is even more pronounced in the friction temperature, θ_* which basically constitutes the ratio between sensible heat flux and friction velocity. As u_* increases and $\langle H_{30} \rangle$ decreases with the surface correlation length, the variation in the friction temperature becomes particularly apparent.

We want to emphasize that the effect of the surface correlation length on the ABL characteristics is neglected by land surface models using MOST with aggregation techniques. Hence, their results may have uncertainties up to 5% as demonstrated at the example of the friction velocity squared. In general, we have reason to suspect even higher uncertainty as our experiments cover only a fraction—up to 650 m—of the variability in the correlation length of surface features. For more general surfaces with even longer surface correlation lengths, higher uncertainties are likely.

To put these results into perspective, we also point out the limitations of our experiment. Having only two land cover classes provides a comprehensible test environment, but in reality the surface structure of permafrost tundra landscapes is obviously much more elaborate. For instance, shrubs have a substantially larger roughness length compared to grassland, thus it can readily be hypothesized that including them in the simulations would augment the impact of fractional changes in land cover elements on the sensible heat flux. Furthermore, it can be expected in reality that the lakes are associated with a substantial latent heat flux that is also not considered in the model but could potentially influence these results.

In order to investigate the fluctuations in the temporospatially averaged parameters and to obtain an estimate for the blending height, we computed the two-dimensional normed SCCF between the sensible heat flux at 30 m and the ground as defined in (5). The SCCF for the experiment with varying lake areal fraction is displayed in Figure 10. In all experiments, the SCCF experiences a peak a few meters off-center with an angle of $17°$ to the x-axis. The peak is shifted down-stream by the mean flow. This shift demonstrates why the SCCF is to be favored against a one-point correlation. The peak values are approximately 0.24 for all the cases independent of the lake areal fraction. Hence, the sensible heat flux at 30 m altitude is arguably uncorrelated from the surface and the surface signal may be considered to be sufficiently blended. Note that the blending height also depends on the background wind. Avissar and Schmidt (1998) concluded that the effects of inhomogeneous surface on the heat
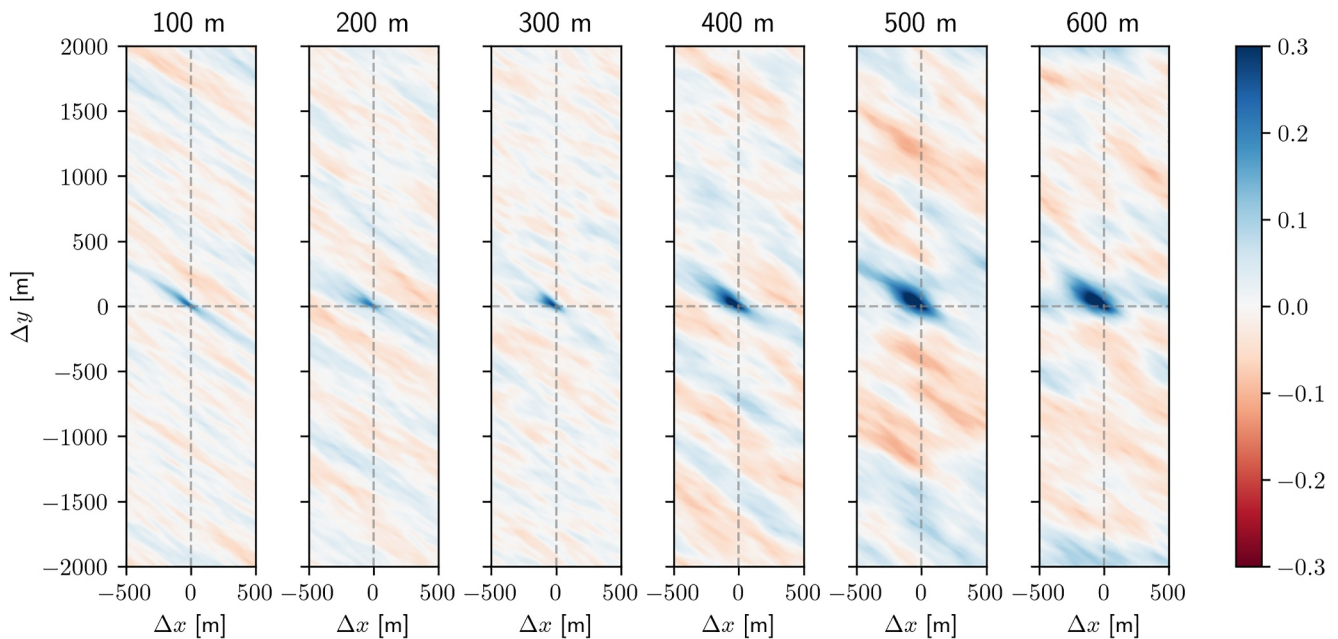
Figure 11. Spatial cross-correlation functions (SCCF) of sensible heat flux at 30 m and the surface, $\varrho_{0,30}$ for large eddy simulations experiments with constant lake areal fraction and altering surface correlation length.

flux is minimized under conditions with a background wind stronger than 5 ms^{-1} which is the approximate value in our experiment at 30 m (cf. Figure 5).

Figure 11 shows the SCCF for the cases with altering surface correlation length. We can also observe shifted peaks. In contrast to the cases with varying lake areal fraction where the peak values were approximately the same, the maximum values do depend on the surface correlation length, here. For $\lambda = 100$ m the peak is about 0.2, that is, reasonably uncorrelated. For $\lambda = 600$ m the peak value exceeds 0.4 which indicates that the surface signal is not sufficiently blended. A larger SCCF implies that the blending altitude is higher. In conclusion, the lake areal fraction does effectively not influence the blending height in our experiments. In contrast, the surface correlation length turns out to have a significant effect on the blending height.

4. Conclusion

By means of LES experiments we were able to demonstrate that the surface heterogeneity has a substantial impact on the ABL in the Arctic permafrost regions due to the extreme differences in surface sensible heat fluxes and surface roughness between vegetated land patches and open water bodies. The Arctic wetting experiment, where we kept the surface correlation length fixed and varied the lake areal fraction, revealed evidence for a feedback mechanism: During snow-free season in the Arctic, permafrost forms tundra lake landscapes typically characterized by alternating patches of grassland and open water bodies as simulated in our experiments. While the albedo of grass is comparatively high, open water bodies are able to absorb ample amount of radiation from the sun causing a negative surface sensible heat flux which cools the air close to the water surface. Along with a decreasing surface water fraction, the aggregated sensible heat flux gets shifted toward higher values and the surface air temperature increases. The increase of temperature, in turn, can cause accelerated thaw which presents a positive feedback.

In contrast to the cases with varying lake areal fraction, experiments with altering surface correlation length have shown a significant impact on the blending altitude. The greater the surface correlation length, the higher the blending altitude. Furthermore, it was demonstrated in the experiments that the inaccuracy in the prediction of the fluxes is up to 5% when neglecting the surface correlation length. These results give a particular incentive to strive for more precise surface heterogeneous metrics in land surface models as these models usually do not include a surface correlation length. A simple but effective remedy in land surface models might be a correction term that takes the surface correlation length derived from remote sensing as an input and is added to the usual prediction by

the tiling method. The correction term may be derived from high-resolution simulations with LES or from scaling arguments.

We note that our stochastic model for the tundra lake landscape is currently based on a simplified setup, as it only provides two land cover classes and the statistics are ad hoc. In an envisioned future investigation, we therefore want to include also shrubs, as their effect on the effective interactions between surface and atmosphere is potentially strong. Due to the design of our surface model using GRFs, this is a feasible task since new land cover classes can be introduced into the model by simply providing new thresholds for the GRF. Also, more realistic statistics will be achieved based on variograms from remote satellite measurements. Representative trajectories in parameter space for permafrost degradation may be achieved.

Another limitation of our model is the lack of air moisture. It can be expected that the surface latent heat flux plays an important role in the ABL dynamics and the surface-atmosphere energy exchange. The EULAG model is capable of moist transport along with the accompanying physics such as clouds (Smolarkiewicz et al., 2017). Furthermore, we assumed a constant heat flux in this study neglecting the diurnal cycle in order to obtain stationary statistics. This limitation can be improved upon. It is planned to perform more realistic studies taking these considerations into account to further inform land surface modelers in their efforts to include permafrost landscapes in ESMs.

Appendix A: Additional Information About the Model Cases

Table A1 gives an overview about the different land cover maps as presented in Figures 2 and 3 in Section 2.3 that were used as an input for the LES runs. It also includes useful statistical measures like mean lake size and number of lakes per square kilometer. A similar table derived from satellite observations is provided by Muster et al. (2019, Table 1). The statistics of the stochastically generated lakes compare well with the real tundra lakes.

Table A1
Parameter Sweep—Definition of Model Runs

Name $QqL\lambda$	Lake areal fraction q [%]	Surface correlation length λ [m]	Mean lake size [km^2]	# Of lakes per km^2
Q05L300	5	300	0.0027	18
Q10L300	10	300	0.0037	27
Q15L300	15	300	0.0056	27
Q20L300	20	300	0.0072	28
Q25L300	25	300	0.0099	25
Q30L300	30	300	0.0160	19
Q10L100	10	100	0.0005	228
Q10L200	10	200	0.0019	53
Q10L300	10	300	0.0037	27
Q10L400	10	400	0.0067	15
Q10L500	10	500	0.0130	8
Q10L600	10	600	0.0180	6

Appendix B: Model Validity, Power Spectral Density

Figure B1 displays the power spectral density for the reference simulation Q10L300 after 12 hr spin-up as defined in Section 2.3 and Appendix A. The inertial sub-range can clearly be observed with the typical slope of $-5/3$ in the log-log plot. In the viscous sub-range, which is dominated by the enstrophy cascade, a kink is present for small wavelengths in the meter range. This kink originates from the turbulence parametrization. Notice that despite this numerical artifact, EULAG is energy consistent, that is, the kinetic energy which is dissipated into heat enters the evolution equation for potential temperature as a source term reflecting the physical process of viscous heating.
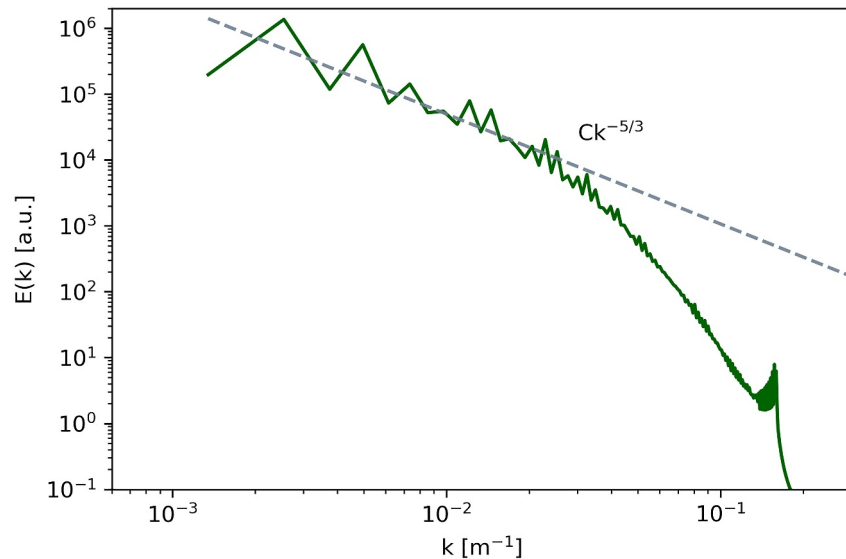
Figure B1. Power spectral density for the Q10L300 simulation after 12 hr. The dashed line represents the inertial sub-range with its typical slope.

Appendix C: Alternative Regression Method for Parameter Sweeps

In Section 3.2, we use a linear best fit curve to analyze the model results. The best fit is produced using the least square method which is known to be sensitive to outliers. Therefore, we also tested a robust regression method: RANSAC (Fischler & Bolles, 1981). The differences between least square and RANSAC (not shown here) were negligible.

Data Availability Statement

The complete primary model output data that was used to produce all figures and analysis is published and made available on https://zenodo.org, see Schlutow et al. (2024).

References

Abramowitz, M., & Stegun, I. A. (1972). Handbook of mathematical functions: With formulas, graphs, and mathematical tables. *Courier Corporation*.
Achatz, U., Klein, R., & Senf, F. (2010). Gravity waves, scale asymptotics and the pseudo-incompressible equations. *Journal of Fluid Mechanics*, *663*, 120–147. https://doi.org/10.1017/S0022112010003411
Avissar, R., & Schmidt, T. (1998). An evaluation of the scale at which ground-surface heat flux patchiness affects the convective boundary layer using large-eddy simulations. *Journal of the Atmospheric Sciences*, *55*(16), 2666–2689. https://doi.org/10.1175/1520-0469(1998)055⟨2666: AEOTSA⟩2.0.CO;2
Blyth, E. M., Arora, V. K., Clark, D. B., Dadson, S. J., De Kauwe, M. G., Lawrence, D. M., et al. (2021). Advances in land surface modelling. *Current Climate Change Reports*, *7*(2), 45–71. https://doi.org/10.1007/s40641-021-00171-5
Bou-Zeid, E., Anderson, W., Katul, G. G., & Mahrt, L. (2020). The persistent challenge of surface heterogeneity in boundary-layer Meteorology: A review. *Boundary-Layer Meteorology*, *177*(2/3), 227–245. https://doi.org/10.1007/s10546-020-00551-8
Bou-Zeid, E., Meneveau, C., & Parlange, M. B. (2004). Large-eddy simulation of neutral atmospheric boundary layer flow over heterogeneous surfaces: Blending height and effective surface roughness. *Water Resources Research*, *40*(2). https://doi.org/10.1029/2003WR002475

Chen, X., Liang, S., & Cao, Y. (2016). Satellite observed changes in the Northern Hemisphere snow cover phenology and the associated radiative forcing and feedback between 1982 and 2013. *Environmental Research Letters*, *11*(8), 084002. https://doi.org/10.1088/1748-9326/11/8/084002

Davies, T., Staniforth, A., Wood, N., & Thuburn, J. (2003). Validity of anelastic and other equation sets as inferred from normal-mode analysis. *Quarterly Journal of the Royal Meteorological Society*, *129*(593), 2761–2775. https://doi.org/10.1256/qj.02.1951

Deardorff, J. W. (1974). Three-dimensional numerical study of the height and mean structure of a heated planetary boundary layer. *Boundary-Layer Meteorology*, *7*(1), 81–106. https://doi.org/10.1007/BF00224974

Dörffel, T., Papke, A., Klein, R., Ernst, N., & Smolarkiewicz, P. K. (2021). Dynamics of tilted atmospheric vortices under asymmetric diabatic heating. *Theoretical and Computational Fluid Dynamics*, *35*(6), 831–873. https://doi.org/10.1007/s00162-021-00591-x

Durran, D. R. (1989). Improving the anelastic approximation. *Journal of the Atmospheric Sciences*, *46*(11), 1453–1461. https://doi.org/10.1175/1520-0469(1989)046⟨1453:ITAA⟩2.0.CO;2

Durran, D. R., & Klemp, J. B. (1983). A compressible model for the simulation of moist mountain waves. *Monthly Weather Review*, *111*(12), 2341–2361. https://doi.org/10.1175/1520-0493(1983)111⟨2341:ACMFTS⟩2.0.CO;2

Fischler, M. A., & Bolles, R. C. (1981). Random sample consensus: A paradigm for model fitting with applications to image analysis and automated cartography. *Communications of the ACM*, *24*(6), 381–395. https://doi.org/10.1145/358669.358692

Foken, T. (2008). *Micrometeorology*. Springer. https://doi.org/10.1007/978-3-540-74666-9

Heße, F., Prykhodko, V., Schlüter, S., & Attinger, S. (2014). Generating random fields with a truncated power-law variogram: A comparison of several numerical methods. *Environmental Modelling & Software*, *55*, 32–48. https://doi.org/10.1016/j.envsoft.2014.01.013

Huang, H.-Y., & Margulis, S. A. (2009). On the impact of surface heterogeneity on a realistic convective boundary layer. *Water Resources Research*, *45*(4). https://doi.org/10.1029/2008WR007175

Jones, B. M., Grosse, G., Farquharson, L. M., Roy-Léveillée, P., Veremeeva, A., Kanevskiy, M. Z., et al. (2022). Lake and drained lake basin systems in lowland permafrost regions. *Nature Reviews Earth & Environment*, *3*(1), 85–98. https://doi.org/10.1038/s43017-021-00238-9

Jungclaus, J. H., Lorenz, S. J., Schmidt, H., Brovkin, V., Brüggemann, N., Chegini, F., et al. (2022). The ICON Earth system model version 1.0. *Journal of Advances in Modeling Earth Systems*, *14*(4), e2021MS002813. https://doi.org/10.1029/2021MS002813

Klein, R., Achatz, U., Bresch, D., Knio, O. M., & Smolarkiewicz, P. K. (2010). Regime of validity of soundproof atmospheric flow models. *Journal of the Atmospheric Sciences*, *67*(10), 3226–3237. https://doi.org/10.1175/2010JAS3490.1

Kurowski, M. J., Wojcik, D. K., Ziemianski, M. Z., Rosa, B., & Piotrowski, Z. P. (2016). Convection-permitting regional weather modeling with COSMO-EULAG: Compressible and anelastic solutions for a typical westerly flow over the alps. *Monthly Weather Review*, *144*(5), 1961–1982. https://doi.org/10.1175/MWR-D-15-0264.1

Liljedahl, A. K., Boike, J., Daanen, R. P., Fedorov, A. N., Frost, G. V., Grosse, G., et al. (2016). Pan-Arctic ice-wedge degradation in warming permafrost and its influence on tundra hydrology. *Nature Geoscience*, *9*(4), 312–318. https://doi.org/10.1038/ngeo2674

Lipps, F., & Hemler, R. (1982). A scale analysis of deep moist convection and some related numerical calculations. *Journal of the Atmospheric Sciences*, *39*(10), 2192–2210. https://doi.org/10.1175/1520-0469(1982)039⟨2192:ASAODM⟩2.0.CO;2

Lohou, F., Druilhet, A., & Campistron, B. (1998). Spatial and temporal characteristics of horizontal rolls and cells in the atmospheric boundary layer based on radar and in situ observations. *Boundary-Layer Meteorology*, *89*(3), 407–444. https://doi.org/10.1023/A:1001791408470

Lupascu, M., Welker, J. M., Seibt, U., Maseyk, K., Xu, X., & Czimczik, C. I. (2014). High Arctic wetting reduces permafrost carbon feedbacks to climate warming. *Nature Climate Change*, *4*(1), 51–55. https://doi.org/10.1038/nclimate2058

Mahrt, L. (2000). Surface heterogeneity and vertical structure of the boundary layer. *Boundary-Layer Meteorology*, *96*(1), 33–62. https://doi.org/10.1023/A:1002482332477

Margairaz, F., Pardyjak, E. R., & Calaf, M. (2020). Surface thermal heterogeneities and the atmospheric boundary layer: The relevance of dispersive fluxes. *Boundary-Layer Meteorology*, *175*(3), 369–395. https://doi.org/10.1007/s10546-020-00509-w

Margolin, L. G., Smolarkiewicz, P. K., & Sorbjan, Z. (1999). Large-eddy simulations of convective boundary layers using nonoscillatory differencing. *Physica D: Nonlinear Phenomena*, *133*(1), 390–397. https://doi.org/10.1016/S0167-2789(99)00083-4

Maronga, B., & Raasch, S. (2013). Large-eddy simulations of surface heterogeneity effects on the convective boundary layer during the LITFASS-2003 experiment. *Boundary-Layer Meteorology*, *146*(1), 17–44. https://doi.org/10.1007/s10546-012-9748-z

McGuire, A. D., Lawrence, D. M., Koven, C., Clein, J. S., Burke, E., Chen, G., et al. (2018). Dependence of the evolution of carbon dynamics in the northern permafrost region on the trajectory of climate change. *Proceedings of the National Academy of Sciences*, *115*(15), 3882–3887. https://doi.org/10.1073/pnas.1719903115

McKay, D. I. A., Staal, A., Abrams, J. F., Winkelmann, R., Sakschewski, B., Loriani, S., et al. (2022). Exceeding 1.5°C global warming could trigger multiple climate tipping points. *Science*, *377*(6611). https://doi.org/10.1126/science.abn7950

Michaelis, J., Lüpkes, C., Zhou, X., Gryschka, M., & Gryanik, V. M. (2020). Influence of lead width on the turbulent flow over sea ice leads: Modeling and parametrization. *Journal of Geophysical Research: Atmospheres*, *125*(15), e2019JD031996. https://doi.org/10.1029/2019JD031996

Miner, K. R., Turetsky, M. R., Malina, E., Bartsch, A., Tamminen, J., McGuire, A. D., et al. (2022). Permafrost carbon emissions in a changing Arctic. *Nature Reviews Earth & Environment*, *3*(1), 55–67. https://doi.org/10.1038/s43017-021-00230-3

Mishra, U., Hugelius, G., Shelef, E., Yang, Y., Strauss, J., Lupachev, A., et al. (2021). Spatial heterogeneity and environmental predictors of permafrost region soil organic carbon stocks. *Science Advances*, *7*(9). https://doi.org/10.1126/sciadv.aaz5236

Muster, S., Riley, W. J., Roth, K., Langer, M., Cresto Aleina, F., Koven, C. D., et al. (2019). Size distributions of arctic waterbodies reveal consistent relations in their statistical moments in space and time. *Frontiers in Earth Science*, *7*. https://doi.org/10.3389/feart.2019.00005

O'Donnell, J. A., Jorgenson, M. T., Harden, J. W., McGuire, A. D., Kanevskiy, M. Z., & Wickland, K. P. (2012). The effects of permafrost thaw on soil hydrologic, thermal, and carbon dynamics in an Alaskan Peatland. *Ecosystems*, *15*(2), 213–229. https://doi.org/10.1007/s10021-011-9504-0

Ostwald, D., Schneider, S., Bruckner, R., & Horvath, L. (2021). Random field theory-based p-values: A review of the SPM implementation (No. arXiv:1808.04075). *arXiv*.

Piotrowski, Z. P., & Smolarkiewicz, P. K. (2022). A suite of Richardson preconditioners for semi-implicit all-scale atmospheric models. *Journal of Computational Physics*, *463*, 111296. https://doi.org/10.1016/j.jcp.2022.111296

Prandtl, L. (1926). Turbulent flow. In *Technical memorandums* (Vol. 435). National Advisory Committee For Aeronautics.

Rantanen, M., Karpechko, A. Y., Lipponen, A., Nordling, K., Hyvärinen, O., Ruosteenoja, K., et al. (2022). The Arctic has warmed nearly four times faster than the globe since 1979. *Communications Earth & Environment*, *3*(1), 1–10. https://doi.org/10.1038/s43247-022-00498-3

Reick, C. H., Gayler, V., Goll, D., Hagemann, S., Heidkamp, M., Nabel, J. E. M. S., et al. (2021). JSBACH 3 - The land component of the MPI Earth system model. *Documentation of version 3.2.*, 4990986. https://doi.org/10.17617/2.3279802

Schlutow, M., Stacke, T., Dörffel, T., Smolarkiewicz, P. K., & Göckede, M. (2024). Simulation results with the EULAG research model for the publication: Large eddy simulations of the interaction between the atmospheric boundary layer and degrading Arctic permafrost. *Zenodo*. https://doi.org/10.5281/zenodo.11205521

Schneck, R., Gayler, V., Nabel, J. E. M. S., Raddatz, T., Reick, C. H., & Schnur, R. (2022). Assessment of JSBACHv4.30 as land component of ICON-ESM-V1 in comparison to its predecessor JSBACHv3.2 of MPI-ESM1.2 (Preprint). *Climate and Earth system modeling*. https://doi.org/10.5194/gmd-2022-74

Schumann, U. (1991). Subgrid length-scales for large-eddy simulation of stratified turbulence. *Theoretical and Computational Fluid Dynamics*, *2*(5), 279–290. https://doi.org/10.1007/BF00271468

Schuur, E. A., Abbott, B. W., Commane, R., Ernakovich, J., Euskirchen, E., Hugelius, G., et al. (2022). Permafrost and climate change: Carbon cycle feedbacks from the warming Arctic. *Annual Review of Environment and Resources*, *47*(1), 343–371. https://doi.org/10.1146/annurev-environ-012220-011847

Schuur, E. A., & Mack, M. C. (2018). Ecological response to permafrost thaw and consequences for local and global ecosystem services. Annual review of ecology. *Evolution, and Systematics*, *49*(1), 279–301. https://doi.org/10.1146/annurev-ecolsys-121415-032349

Smith, S. L., O'Neill, H. B., Isaksen, K., Noetzli, J., & Romanovsky, V. E. (2022). The changing thermal state of permafrost. *Nature Reviews Earth & Environment*, *3*(1), 10–23. https://doi.org/10.1038/s43017-021-00240-1

Smolarkiewicz, P. K. (2006). Multidimensional positive definite advection transport algorithm: An overview. *International Journal for Numerical Methods in Fluids*, *50*(10), 1123–1144. https://doi.org/10.1002/fld.1071

Smolarkiewicz, P. K., Kühnlein, C., & Grabowski, W. W. (2017). A finite-volume module for cloud-resolving simulations of global atmospheric flows. *Journal of Computational Physics*, *341*, 208–229. https://doi.org/10.1016/j.jcp.2017.04.008

Smolarkiewicz, P. K., Kühnlein, C., & Wedi, N. P. (2014). A consistent framework for discrete integrations of soundproof and compressible PDEs of atmospheric dynamics. *Journal of Computational Physics*, *263*, 185–205. https://doi.org/10.1016/j.jcp.2014.01.031

Smolarkiewicz, P. K., Sharman, R., Weil, J., Perry, S. G., Heist, D., & Bowker, G. (2007). Building resolving large-eddy simulations and comparison with wind tunnel experiments. *Journal of Computational Physics*, *227*(1), 633–653. https://doi.org/10.1016/j.jcp.2007.08.005

Sorbjan, Z. (1996). Numerical study of penetrative and "solid lid" nonpenetrative convective boundary layers. *Journal of the Atmospheric Sciences*, *53*(1), 101–112. https://doi.org/10.1175/1520-0469(1996)053⟨0101:NSOPAL⟩2.0.CO;2

Sühring, M., & Raasch, S. (2013). Heterogeneity-induced heat-flux patterns in the convective boundary layer: Can they be detected from observations and is there a blending height? A large-eddy simulation study for the LITFASS-2003 experiment. *Boundary-Layer Meteorology*, *148*(2), 309–331. https://doi.org/10.1007/s10546-013-9822-1

Wackernagel, H. (1995). *Multivariate geostatistics*. Springer. https://doi.org/10.1007/978-3-662-03098-1